Journal of Alloys and Compounds 910 (2022) 164760

Contents lists available at ScienceDirect

Journal of Alloys and Compounds

journal homepage: www.elsevier.com/locate/jalcom

Influence of processing parameters on density, surface morphologies and hardness of as-built Ti-5Al-5Mo-5V-3Cr alloy manufactured by selective laser melting

Mansur Ahmed[a,*], Muhannad A. Obeidi[b], Shuo Yin[a], Rocco Lupoi[a]

[a] Department of Mechanical, Manufacturing & Biomedical Engineering, Trinity College Dublin, The University of Dublin, Dublin, Ireland
[b] School of Mechanical and Manufacturing Engineering, Dublin City University, Dublin, Ireland

ARTICLE INFO

Article history:
Received 3 November 2021
Received in revised form 8 March 2022
Accepted 23 March 2022
Available online 28 March 2022

Keywords:
Ti alloy
SLM
Surface morphology
Surface roughness
Laser processing parameter
Hardness

ABSTRACT

Demand for new Ti alloys for AM is immense. Ti–5Al–5Mo–5V–3Cr (wt%), a β type Ti alloy is chosen for this study as it possesses excellent properties. Samples are manufactured using SLM technique. Relative density, surface morphologies and hardness of samples produced by varying laser processing parameters, e.g., laser scan speed and laser power, are thoroughly investigated. Top surface of the as-built samples shows adhered powder particles and discontinuous ripple patterns. A change in scan speed from 1200 to 1400 mm.s^{-1} drastically deteriorates top surface quality in terms of ripples patterns and adhered powders. Surface roughness (S_a/R_a) of the side surface of the produced samples shows a value of below 20 μm. Side surfaces show adhered powder particles, open surface pores, microcrack and interlayer crack. Substantial increase in adhered powder particles is evident when both laser power and laser scan speed are increased distinctively. These results are discussed with the help of the thermodynamic and metallurgical phenomena involved in the SLM processing. Hardness of the as-built samples is measured, the value is in agreement with conventional processing. This fundamental study will be useful for producing Ti-5553 alloy AM parts with optimum surface.

1. Introduction

Ti–5Al–5Mo–5V–3Cr (wt%) (Ti-5553) is a near β Ti alloy that has a nominal density of 4.67 gm/cm^3. It offers a very high strength, good ductility, excellent corrosion resistance properties and proved weldability [1–4]. The high strength and good ductility together positively affect fatigue behaviour of Ti-5553 [5]. Due to excellent hardenability, a second phase called hcp Ti phase (α-phase) precipitates from metastable bcc Ti phase (β-phase) during heat treatment. As a result, a two-phase microstructure is achieved which can displays very high ultimate tensile strength of 1.4 GPa. Because of these properties, this alloy has been using in many engineering applications especially aerospace (landing gear and airframe in Boeing 787) and automotive industries [6]. In addition, a recent study shows that it can be a potential candidate for biomedical application especially in bone implantation [7].

Additive manufacturing (AM) technique has already shown a great potential producing near net-shape components. As proven, AM saves both material and machining cost. Selective laser melting (SLM) is one of the popular AM processes that are extensively used in metal applications [8,9]. It is a layer-by-layer technique where a laser system consisting of high laser power is used for melting the powder, and produces parts using the input CAD drawing. To date, two Ti materials (CP Ti and Ti-6Al4V) have attracted significant research interest. Besides, there are Ti alloys that are being used in engineering applications. These motivate us to find new Ti alloys for AM process. Due to the above mentioned excellent properties of Ti-5553, this alloy is chosen for this study. A few studies has been reported on this material focusing build up relationship between processing, microstructure and mechanical properties [10–13].

Regardless of the application, surface of the SLM produced parts is crucial for determining its properties, useability and feasibility. Since this is a new in AM field, the surface morphologies of as-built Ti-5553 alloy need to be thoroughly understood. The present study aims to evolute the surface morphologies of as-built SLM Ti-5553 alloy with respect to laser processing parameters, such as laser power and scanning speed. Surface quality and characteristics of AM

* Correspondence to: Department of Mechanical, Manufacturing and Biomedical Engineering, The University of Dublin, Trinity College, Ireland.
E-mail address: maahmed@tcd.ie (M. Ahmed).

https://doi.org/10.1016/j.jallcom.2022.164760
0925-8388/

parts made of metallic materials are available in the literature [14–21]. Defects and irregularities such as, powder adhered to the surface, surface pores, formation of balling, crack etc are reported [22–24] and they generally impair the mechanical and biomedical performance [25–33]. In most cases, extra effort i.e., surface finish is therefore needed to remove such defects which incurs cost and time [34,35] except osteointegration in bone implants. Such extra time and relating cost is against one of the basic principles of AM. During SLM, several thermodynamic and metallurgical phenomena e.g., viscosity and surface tension of the melt, solidification characteristics etc. [36–40] occur that are responsible for producing defects. Understanding these AM process definitely assists reducing such defects. In this study, we reveals the surface morphologies produced in SLM produced Ti-5553 alloy and their dependence of laser processing parameters.

2. Materials and experimental details

2.1. Material

Sphere-shaped, fully dense, (argon) gas atomised powder particles of Ti-5553 alloy were purchased from TLS Technik, Germany. The range of the diameter of the powder was 20–60 µm. Fig. 1 shows the powder particles distribution analysis. Particle size distribution was analysed using ISO 13320. The value of D_{10}, D_{50}, and D_{90} are calculated to be 28.21, 42.86 and 62.21 µm. The chemical composition of the powder is given in Table 1.

2.2. Experimental details

A SLM system EOS 290, GmbH-Germany is employed to produce the alloy sample. The system contains Yb-fibre laser with a beam focus diameter of 100 µm and a maximum power of 400 W. A protective argon environment enabling high performance is used during sample production. A telecentric f-theta lens attached to the system ensures the laser beam to be perpendicular to the working plane. A wide range of processing parameters are initially used for getting dense samples. Of these, samples with 98% and above relative density are selected for this study. Table 2 shows the laser processing parameters that are used to produce samples for analysing surface morphologies. The volumetric energy density (VED) of each processing parameter is calculated using the following equation.

$$\mathrm{VED} = \frac{\mathrm{P}}{\mathrm{vth}} \tag{1}$$

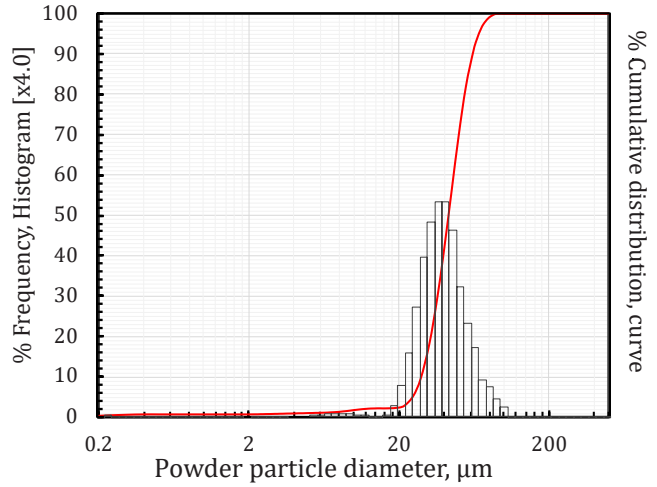

Fig. 1. Powder particle distribution of Ti-5553 alloy powder used in this study.

Table 1
Chemical composition of the Ti-5553 alloy powder used in the study.

Element	Al	Mo	V	Cr	Fe	O	Ti
wt%	5.09	4.92	4.82	3.05	0.44	0.13	Balance

Table 2
Laser processing parameters used in this study.

Laser power (P), W	Scan speed (v), $mm.s^{-1}$	Volumetric Energy density (V.E.D.), J/mm^3
270	1200	75.0
270	1400	64.3
300	1200	83.3
300	1400	71.4
330	1200	91.7
330	1400	78.6

Here, laser power (P), and scan speed (v) are used as variables. A layer thickness (t) of 30 µm and hatch spacing (h) of 100 µm are used for all samples. Commercially pure Ti as substrate at a temperature of 200 °C is used. The scanning strategy follows stripes pattern with 67° rotation for the subsequent layer. Three cubic samples with a dimension of 10 mm × 10 mm × 10 mm each, are fabricated using each testing condition. Fig. 2 shows the photos of the as-built samples. Top and side surfaces of a cube is shown as inset in Fig. 2b. Top surface clearly shows the equally spaced scanning tracks of the laser. Side surface displays accumulation of the powders.

2.3. Surface characterisation

Surface profile is characterised by mean of a 3D optical microscope from Bruker Contour GT. Three different locations with an area of 1.5 mm × 1.5 mm each from each sample are analysed to obtain the surface profile. From the 3D maps acquired, the surface roughness analysis is performed. Both linear roughness (R_a, R_{sk}, R_z) and area roughness (S_a, S_{sk}, S_z) parameters are measured. Values obtained are then statistically averaged.

The surfaces of the as-built samples are characterised using scanning electron microscope (SEM). A field emission SEM (FE-SEM) (Zeiss ULTRA plus GmbH, Germany) equipped with both InLens and SE2 detectors at an acceleration voltage of 5 kV is used for imaging. Both InLens and Secondary electron modes are used for imaging. The adhered powders on the surface are measured using Image J (NIH, USA) using SEM micrograph. A representative area of 3.5 mm × 2.5 mm is used for this purpose.

2.4. Density, Vickers hardness and X-ray diffraction

Density of the as-built samples was measured employing Archimedes method. Following Eq. (2) is applied to calculate the density of the part, (ρ_p):

$$\rho_p = \frac{m_a}{m_a - m_{fl}} \times \rho_{fl} \tag{2}$$

where ρ_{fl} is the density of the fluid, which is dependent on temperature. m_a is the mass of the part in air and m_{fl} is the mass of the part in the fluid. In the present study, deionised water and a customised solution provided by the supplier were used as the fluid. Temperature dependencies of the fluid-density are taken into account. Three samples from each condition and four times from each sample were independently measured. Then, average of the twelve readings is taken.

A ZwickRoell Indentec Vickers hardness tester was employed to measure Vickers hardness of the samples. 5 kg load for a dwell time of 10 s was applied on the surface of samples. At least, ten readings from each sample was taken for statistical significance. The distance

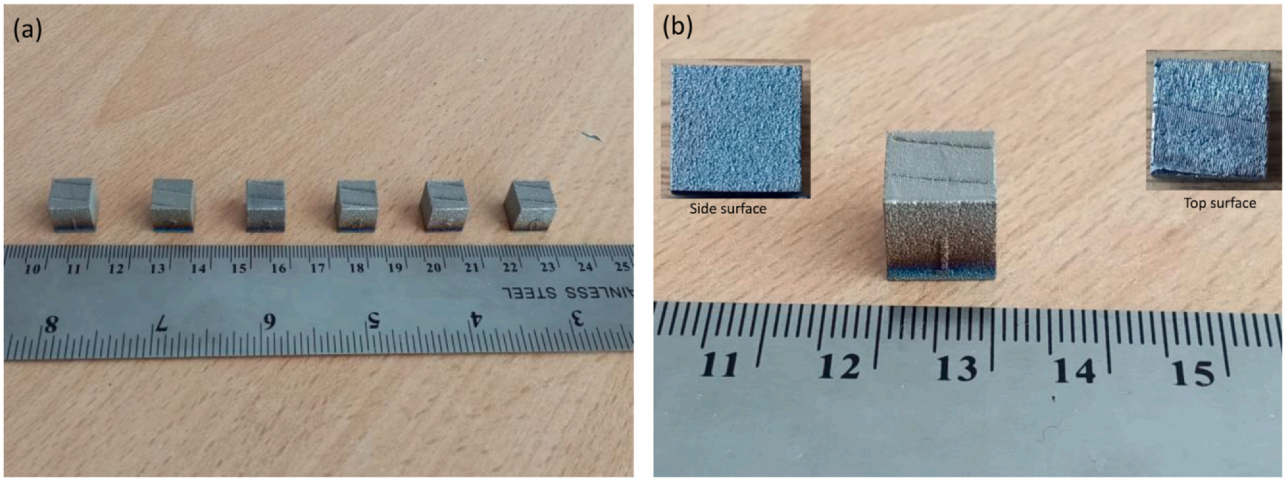

Fig. 2. (a) Photos of as-printed samples investigated in this study. (b) Higher magnification images of top surface and side surface of a sample.

between two indentation was carefully maintained to avoid impression of each other.

A PANalytical X'Pert PRO Multipurpose diffractometer (MPD) with Cu Kα radiation (λ = 0.154 nm) filtered with Ni-monochromator X-ray diffraction investigations were employed at 45 mA and 40 kV. Continuous scanning mode over the 2θ range of 30–100°, with 0.01° step size and 490 s resulting acquisition time was used for scanning. A standard polycrystalline silicon sample was used to characterise the instrumental broadening. Both top and side surfaces were used for XRD scanning.

3. Results and discussion

3.1. Density and surface roughness parameters

Density becomes one of the priority parameters to understand the build quality. As mentioned, all studied conditions display a relative density of over 99% implying that the chosen processing parameter settings are effective for producing fully dense parts (Fig. 3). The change in laser power and scanning speed has negligible impact on density. It means Ti-5553 alloy has a wide processing range (VED) from 64.3 to 91.7 J/mm^3 for producing a dense parts that is a one of keys in AM. Fig. 4 displays a surface topography map of one of the side surfaces of a sample manufactured using 270 W, 1200 mm.s^{-1}. Based on the 3D surface topography image, surface roughness parameters have been computed. As the S_a and R_a are the

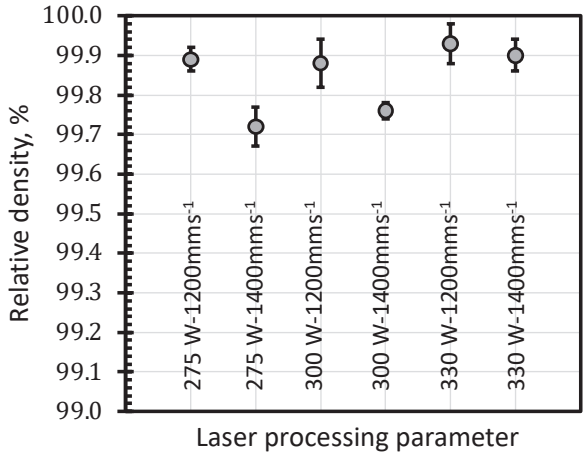

Fig. 3. Relative density of Ti-5553 alloy sample produced in this study.

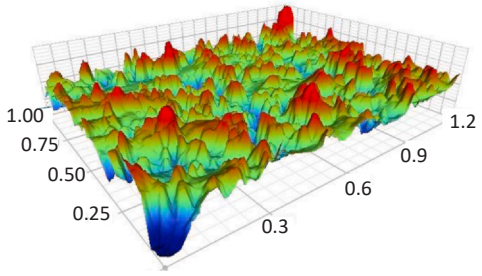

Fig. 4. A representative surface topography map of a side surface of as-built Ti-5553 alloy.

most typical parameters to describe a surface quality, the evolution of S_a and R_a as functions of laser power and scanning speed is shown in Fig. 5. It is noted that highest values of S_a and R_a obtained for side surface of the as-built Ti-5553 alloy are below 20 µm. Similar results of S_a and R_a have been reported in [7]. Lowest S_a (16.7) and R_a (16) are found for 300/1400 and 300/1200 samples, respectively. However, the variation of S_a and R_a with respect to laser power and scanning speed cannot be formulated. The results of S_a and R_a also imply that the VEDs do not impact surface roughness much. Other roughness parameters such as S_{sk}, R_{sk}, S_z and R_z are summarised in Table 3. Negative R_{sk} values are seen for higher scanning speed (1400 mm.s^{-1}) for all investigated laser powers. It means the peaks of the surfaces are not symmetrical from valleys. On the other hand, maximum total height of the peak obtained by areal method (S_z) ranges from 156 to 183 µm whereas linear method (R_z) returns a value between 91 and 107 µm. It is evident that 300 W,1200 mm.s^{-1} sample gives lowest total height (S_z and R_z).

During SLM processing, following three factors can be considered to affect surface quality of a metallic as-built sample.

(1) Formation of balling and its effect
(2) Stair-step effect
(3) Powder particle size distribution

Formation of balling is observed on the surface of the as-built sample. It is known that such balling contributes to the surface roughness. As shown in later section, the balling formation in this study is not pronounced and hence, its effect toward surface roughness can be regarded less contributing. Given the simple cubic shape and building strategy, the stair-step effect has negligible contribution to surface roughness produced in this study. On the other hand, particle size distribution of the Ti-5553 powder used

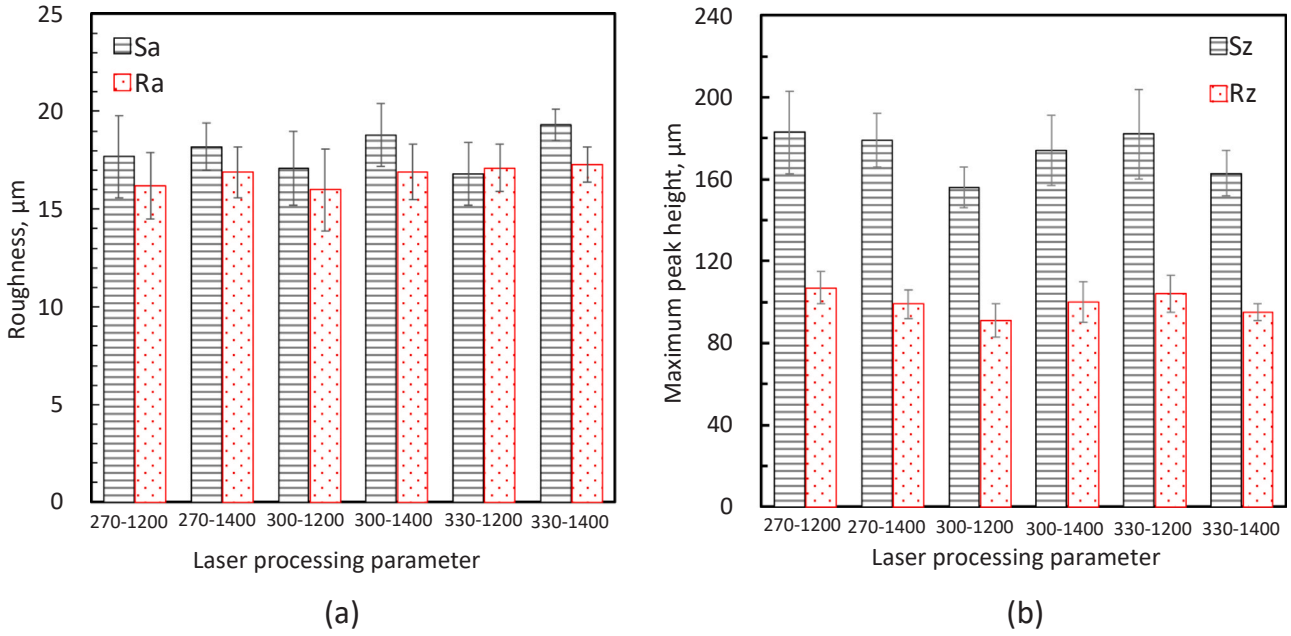

Fig. 5. Surface roughness parameters: (a) surface roughness (S_a and R_a) and (b) maximum peak height (S_z, and R_z) with respect to laser processing parameters.

Table 3
Surface roughness parameters of as-built Ti-5553 alloy.

Sample (W/mm.s^{-1})	Skewness (S_{sk})	Max. height (S_z), µm	Skewness (R_{sk})	Max. height (R_z), µm
270/1200	-0.21	183	0.01 ± 0.7	107 ± 28
270/1400	0.08	179	-0.18 ± 0.4	99 ± 17
300/1200	0.15	156	0.12 ± 0.5	91 ± 18
300/1400	-0.16	174	-0.12 ± 0.5	100 ± 22
330/1200	0.52	182	0.32 ± 0.7	104 ± 24
330/1400	0.17	163	-0.02 ± 0.4	95 ± 14

significantly contributes to the surface quality. The formation of peaks and valleys of various heights is occurred through poor powder settling on the build substrate when a vastly scattered powder particle size distribution is used. Zopp et al. [41] illustrated that the surface quality in terms of heights (R_z) is dependent on powder particle size distribution. For instance, finer powder distribution (25–32 µm) leads to better surface quality (R_z = 69 µm) compared to R_z = 109 µm for coarser size powders (53–63 µm). In this study, we have used a wide range of powder feedstock (20–60 µm) and therefore, a value of R_z between 69 and 109 µm is expected. Further, for a particular powder range, different surface

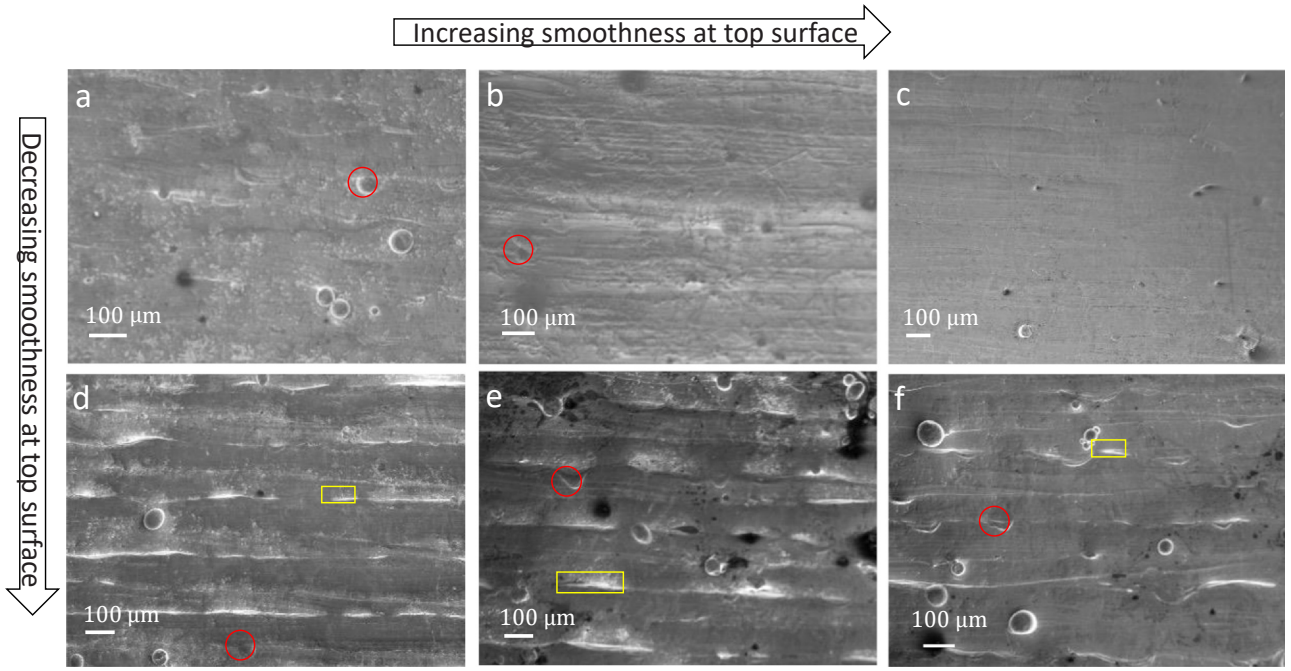

Fig. 6. Top surface: Micrograph of samples produced at (a) 270 W/1200 mm.s^{-1}, (b) 300 W/1200 mm.s^{-1}, (c) 330 W/1200 mm.s^{-1}, (d) 270 W/1400 mm.s^{-1}, (e) 300 W/1400 mm.s^{-1} and (f) 330 W/1400 mm.s^{-1}. Red circles indicate partially melted powder particles. Yellow rectangles show the white contrast produced due to the elevation between two nearby scanning tracks i.e., ripple pattern.

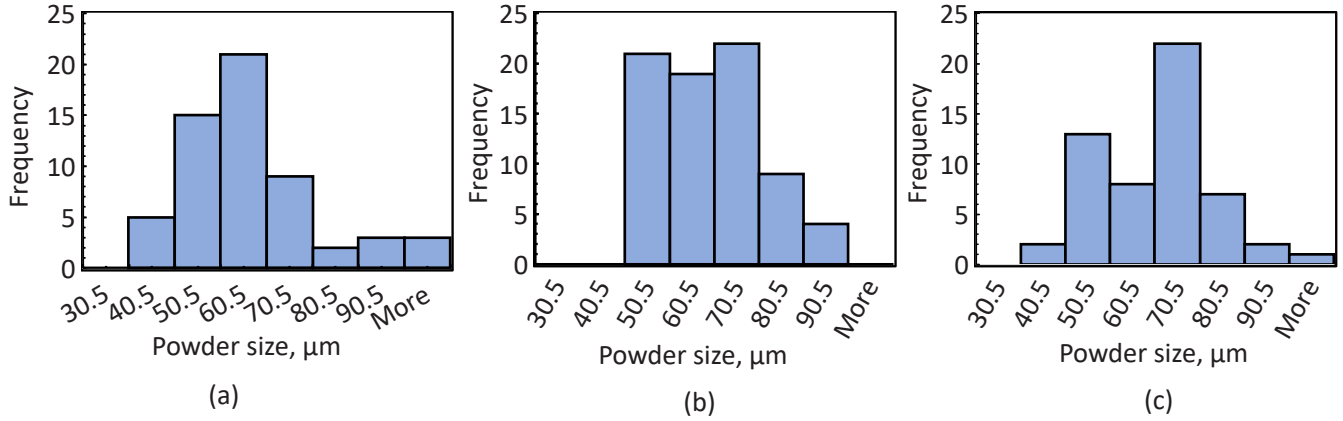

Fig. 7. Powder size distribution of the adhered powders present on the top surfaces of samples produced using (a) 270 W/1400 mm.s^{-1}, (b) 300 W/1400 mm.s^{-1}, (c) 330 W/1400 mm.s^{-1}.

quality is achievable by employing various laser parameters i.e., VEDs. The obtained R_z (91–107 µm) in this study clearly indicates the dependence of powder size range of surface quality in association to SLM processing parameters.

3.2. Surface morphologies using various process parameters

3.2.1. Characterisation of top surfaces

Fig. 6 shows the top surfaces of the samples manufactured using different laser processing parameters. It is evident that the smoothness of the top surface drastically deteriorates when the scan speed increases from 1200 to 1400 mm.s^{-1} for all laser power conditions (Fig. 6a vs. d, b vs. e and c vs. e). Here, smoothness is termed as the presence of adhered powder particles and ripples. Very few powder particles are seen on the top surface of samples manufactured at 1200 mm.s^{-1}. In contrast, substantial powder particles are clearly visible on the samples produced at 1400 mm.s^{-1}. These include droplet spatter, splash spatter and melted particles. Number of particles adhered to the top surfaces of samples produced at 1400 mm.s^{-1} is counted, and found to be approximately equal in number. Powder particles distribution for the samples manufactured at 1400 mm.s^{-1} is given in Fig. 7. Various size powder particles are obtained. There are powder particles with size greater than that of the raw power size used. This phenomenon indicates balling formation through droplet spatter. The elevation difference between two adjacent scanning tracks represents ripple, shown as yellow boxes. Ripples are seen for all samples at 1400 mm.s^{-1}. It is pertinent mentioning that ripples are discontinuous in these samples.

On the other hand, smoothness is marginally increased with increased laser power from 270 to 300–330 W for both speed conditions (Fig. 6a vs. b vs. c, and d vs. e vs. f). In terms of adhered powder and ripples, the change is not substantial with respect to laser powers for both scan speeds. Possibly, the change in VEDs with laser power is not adequate to have a notable change in top surface morphology. Further study with higher laser power difference is required to find such a relation.

In this circumstance, the variation in top surface morphology with respect to laser scan speed is discussed. Interrelation between processing parameters, i.e., VED, and viscosity can be used to explain. As known, melt pool viscosity is inversely proportional to VED, i.e., the viscosity of the melt pool decreases with an increase in VED [40]. Additionally, the increased scanning speed hinders dispersion of the melt properly as lesser time is given against viscous drags [39]. Due to lower VEDs with increased scan speed, the viscosity of the molten materials of the samples manufactured at 1400 mm.s^{-1} is higher than that of the samples made at the scanning speed of 1200 mm.s^{-1}. As a result, the surface tension becomes higher at samples produced at 1400 mm.s^{-1}. To decrease such surface tension, the materials forms balls resulting in balling formation. Small droplets and big splash spatters also produce, which adhere to the top surface of the sample [42]. At higher scanning speed, a higher rate of raw powder particles spatters, which also adds to the adhered powder on the top of the samples. The results obtained in this study supports the above description, and shows a higher amount of adhered powder on the top surfaces of samples manufactured at 1400 mm.s^{-1} than that of samples made at 1200 mm.s^{-1}.

A variation in surface temperature between the solidifying zone and the action zone occurs during laser beam movement. This phenomenon also induces surface tension. A rippling influence is found on the top of the melt pool through the shear force resulting from such surface tension [35,43]. At higher scan speed of 1400 mm.s^{-1}, the laser moves faster than the scan speed of 1200 mm.s^{-1}, and hence, generates higher surface tension which gives more shear force. Thus, observed ripples at 1400 mm.s^{-1} samples are fully justified. As a result of the higher amount of adhered powder and ripples, the smoothness of the samples at 1400 mm.s^{-1} becomes worse.

3.2.2. Characterisation of side surfaces

Fig. 8 shows the overview of side surfaces of the samples printed in this study. The characteristics of these surfaces include adhered powders, stacked powder, surface gap and formation of balling, and open surface pores. Partially-melted, fully-melted, and unmelted powders are visible in the surfaces. It is evident that the number of adhered powder increases with increased laser power (Fig. 8a vs. b and c vs. d) (Table 4). This is observed for both scanning speeds. At a constant scanning speed, with increasing laser power, the energy due to the laser heat per unit time increases. Higher energy produced at higher laser power drags more powder particles due to the capillary force and then melts on the side surface [22,44]. In addition, cyclone-like environment is created in the melt pool. Such rigorous environment assists in adherence of powder particle to the melt pool surface through attraction and progression of powder particles to the surface [45,46]. Hence, more powders are visible on side surface of sample produced at 330 W, 1200 mms^{-1} than that of 270 W, 1200 mms^{-1}, and of 330 W, 1400 mms^{-1} than that of 270 W, 1400 mms^{-1}. Further, the VED increases with increased laser power. At higher VED, more powders attached to the surface near the scanning track do liquefy. In addition, surface tension slope and the Marangoni effect are evolved due to the sharp thermal gradient at

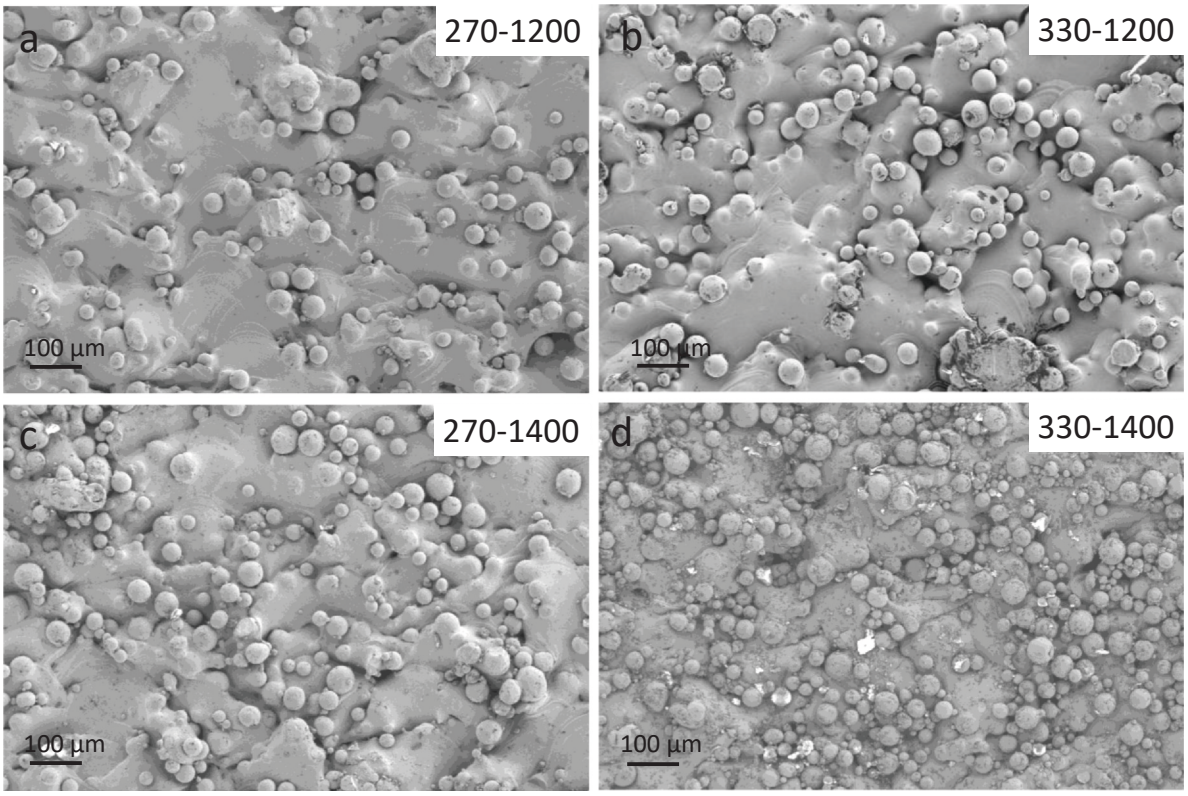

Fig. 8. Side surfaces of the samples manufactured using various laser powers and scanning speeds (a) 270 W/1200 mm.s^{-1} and (b) 330 W/1200 mm.s^{-1}, (c) 270 W/1400 mm.s^{-1} and (d) 330 W/1400 mm.s^{-1}.

Table 4
Powder particles on the sides surfaces.

Sample (W/mm.s^{-1})	Total powder particles (number/mm^2)
270/1200	100 ± 7
270/1400	167 ± 12
300/1200	124 ± 6
300/1400	198 ± 13
330/1200	156 ± 10
330/1400	328 ± 14

higher VED. These events together detach the melt pool, and approve the balling effect [27]. As a result, we have seen higher balling formation in the sample manufactured at 330 W, 1400 mm.s^{-1} (Fig. 9a).

The number of adhered powder particles also increases with increased scanning speed when the laser power remains unchanged (Fig. 8a vs. c and b vs. d) (Table 4). At a constant laser power, the VED decreases with increased scan speed. Lower VED makes melt pool more viscous that attracts powder particles to the side surface. Of the powders, a large amount of the powders do not dissolve due to rapid cooling at higher scanning speed. Therefore, the presence of higher adhered powders on the side surface of at higher scanning speed is justified. Additionally, high viscous melt shows characteristics of reduced wettability and fluidity. These make the liquid difficult from penetrating the powders [28]. A poor bonding between the side surface of the sample and the adhered powder particles is reported to occur [29].

In addition to the adhered powders, other defects can be also seen on the side surfaces that are of particular interest (Fig. 9). Small gaps/pores on the surface is also seen. The size of these pores ranges between 15 and 35 µm and the depth of the pore are about 10 µm (Inset of Fig. 8a). These pores may act as crack initiation point and hence deteriorate surface sensitive mechanical properties like fatigue. Powder stacking is found on the surface. Equally spaced ripples (a size of about 5 µm) can be seen on the surface.

In SLM technique, it is generally known, more energy is produced in the centre of the melt pool than that of the adjacent heating zone. This creates a variation in viscosity between the centre and the circumference side. Thus, a steep thermal slope is occurred that creates a high Marangoni effect. As a result of such Marangoni effect, the melt radially moves inside the melt pool [47]. Some adhered and partially melted powders move inside of the melt pool and stay there as partially melted powders. In such a condition, at higher scanning speed, the trapped partially melted powders cool slower compared to the melt pool. Then, during solidification, the melt pool shrinks quicker than that of the partially melted powder particles inside the melt pool. This is because of the discrepancy in thermal coefficient of the two states. Consequently, microcracks evolves at the interfaces of powder particle and molten material. In the present study, microcracks marked by blue arrows are seen on the side surfaces in Fig. 10. Microcracks are pronouncedly noticed in samples manufactured at higher power (330 W) with higher scanning speed (1400 mm.s^{-1}). Possible powder particles responsible for the cracks are shown as circles. The diameter of these powder particles is around 30 µm or larger, and more than half of each particle involves in the cracking are located in the melt pool. It implies that these powders did solidify inside of the melt pool, which creates a great variation in shrinking tension between the powder and the melt pool. Hence, microcrack evolves. The horizontal appearance of the cracks is another important feature of the observed crack characteristics. This phenomenon is attributed to the melt pool cooling and solidification characteristics. For instance, a melt pool cools and solidifies from bottom to top [36] due to the difference in rate of heat

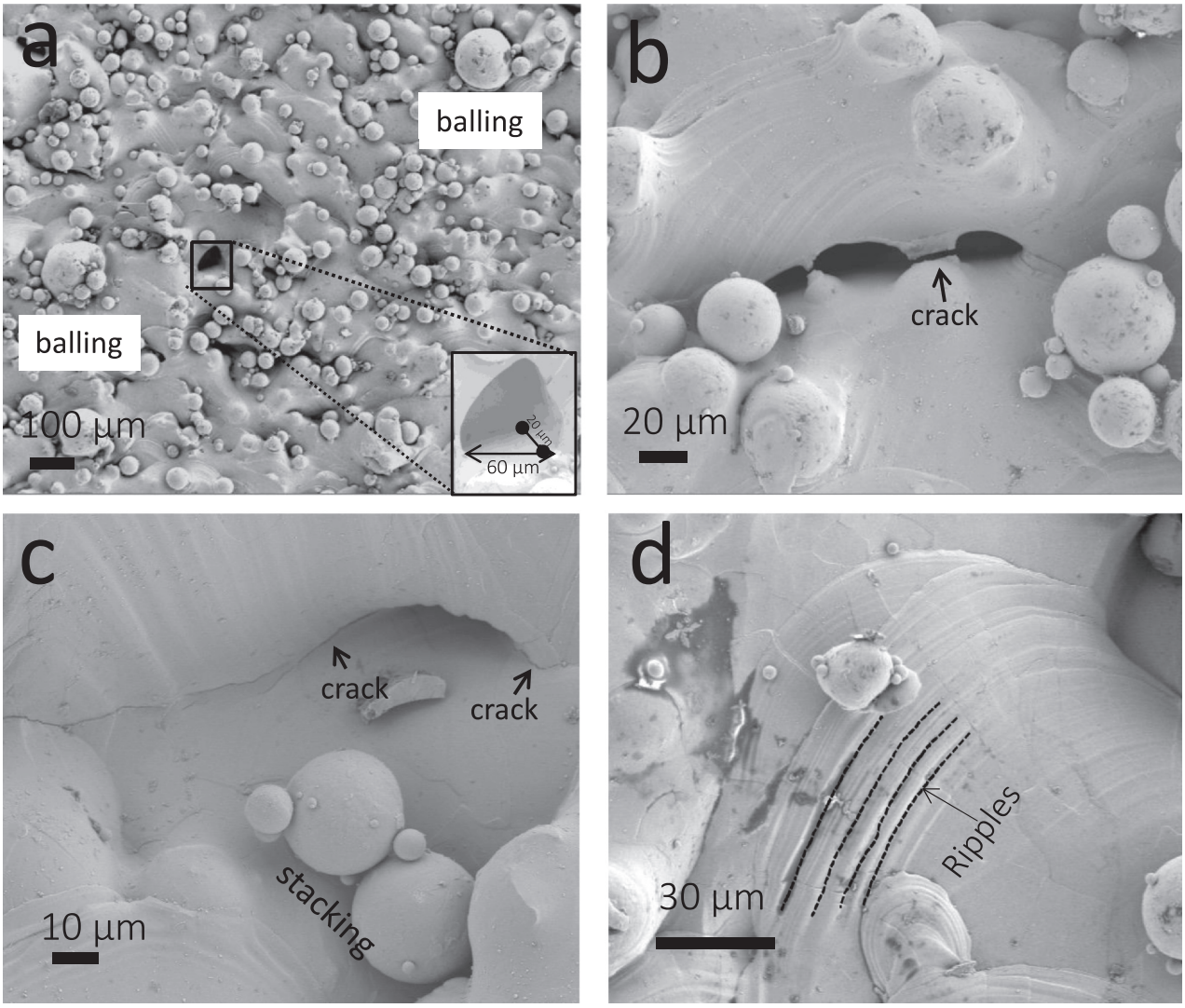

Fig. 9. Some defects (a) formation of balling, (b) open surface pores (c) crack originating from the open pore (d) ripples observed in the samples.

transfer between the powder particles and the melt pool. As known, solid material has faster thermal coefficient than the liquid, i.e., powder particles conducts heat faster than the melt pool using convection process and hence, the shrinking of melt pool occurs from bottom to top. During the shrinking process, the cracks evolves horizontally at the interface when the melt located below the powder particle starts solidification and shrinking given the powder stays stagnant. It is worth mentioning that majority of the adhered powder particles did not participate in crack formation. The high affinity of Ti toward oxygen is well known especially at high temperature and could be used as possible explanation in crack formation. During SLM processing, at high temperature, Ti can attract oxygen and form oxidation although inert atmosphere is ensured within the chamber to resist such incidence [48]. Such oxidation might impact in crack formation [49].

Fig. 11 shows another type of crack called inter-layer crack. This crack is seen in samples produced at the scanning speed of 1400 mm.s^{-1}. At 1400 mm.s^{-1}, both the VED of the melt pool and cooling time reduce. Simultaneously, the input energy also reduces, and, thus, the melt pool viscosity becomes higher. Thus, a higher amount of powder particles is supposed to be adhered to the melt pool. However, reduced laser input cannot melt the adhered powders adequately. In such circumstance, the rapid cooling due to higher scanning speed causes crack at the interface between layers. The observed interlayer cracks ranges from 40 to 100 µm. It can be classified as middle size crack, which gives an indication that further increase in scanning speed would produce larger crack.

3.3. Hardness of the as-built Ti-5553

Vickers hardness number (VHN) of the top surfaces of the Ti-5553 alloy samples is measured to be in the range from 270 ± 20–288 ± 11 (Fig. 12). The processing parameters shows very little influence on the VHN that can be ignored. It can be attributed to insignificant changes in the VED due to laser power and scanning speed variation to alter the internal microstructure. Further, a very high relative density of the samples acquired is a contributing factor. VHN of the Ti-5553 alloy produced via conventional processing varies from 290 to 470 depending on the presence of constituent phases [50]. Single β phase after solution treatment gives lower hardness value of about 300 VHN whereas the presence of α phase and ω phase increases hardness to a value of 470 VHN. Our hardness value of SLM Ti-5553 alloy is in good agreement with the conventionally processed material and also

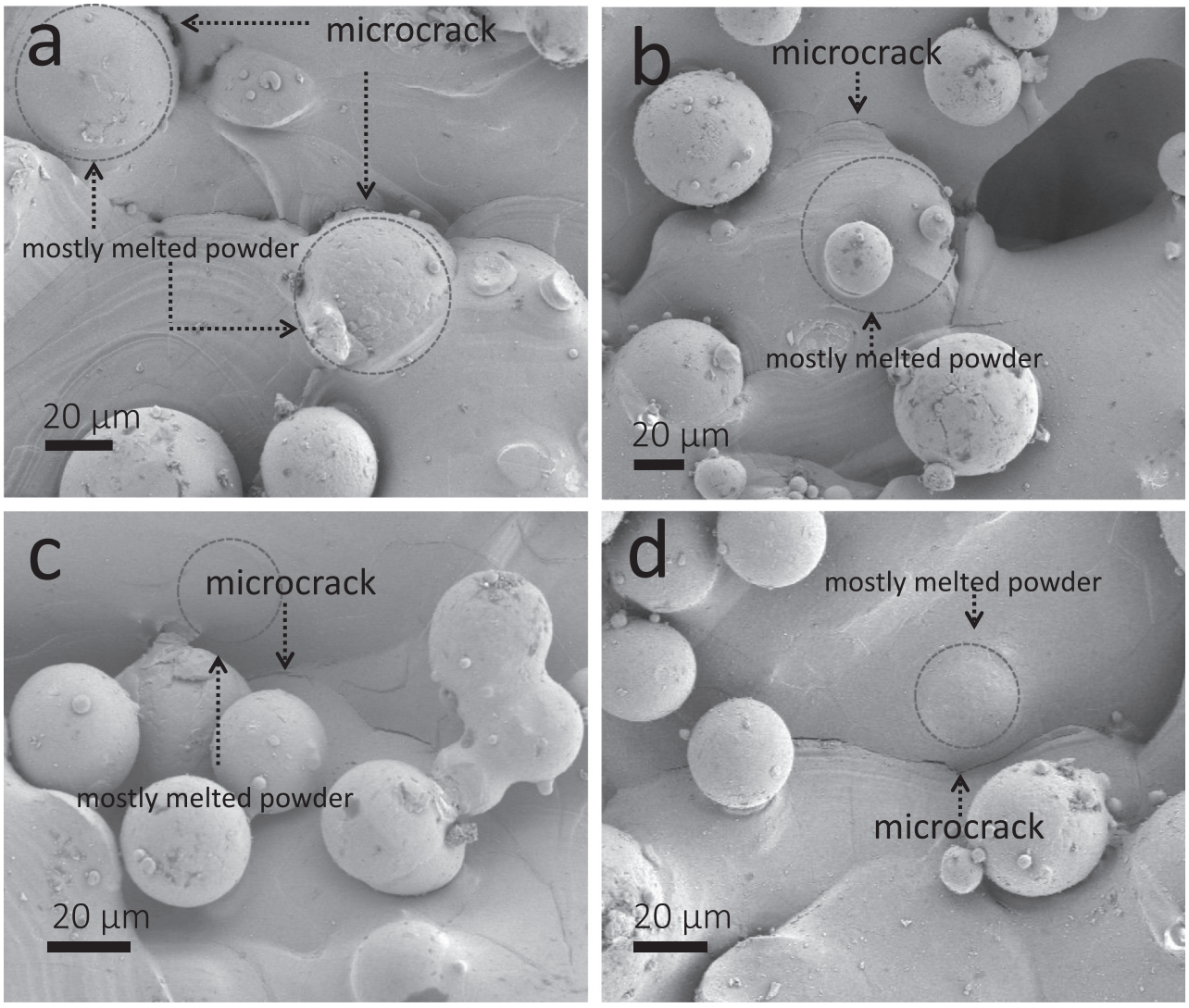

Fig. 10. Microcracks in the samples manufactured at (a) 270 W/1200 mm.s^{-1} (b) 300 W/1200 mm.s^{-1} (c) 300 W/1400 mm.s^{-1} (d) 330 W/1400 mm.s^{-1}. Circles indicate the melted powder particles those in association with laser processing parameters are responsible for crack formation.

indicates that microstructure of the as-built Ti-5553 consists of single β phase parts. To further confirm, XRD patterns of the samples are obtained (Fig. 13). It is evident that single β phase is found in the samples for all studied conditions. This supports the finding of epitaxial/elongated β grains in microstructure of SLM Ti-5553 alloy by Schwab et al. [12]. However, it does not support the claim that microstructure of SLM Ti-5553 alloy consists of nano-scale α in association epitaxial/elongated β grains [51]. Similar to top surfaces, side surfaces also display similar VHN level. A higher VHN of about 350 is obtained when the indenter places

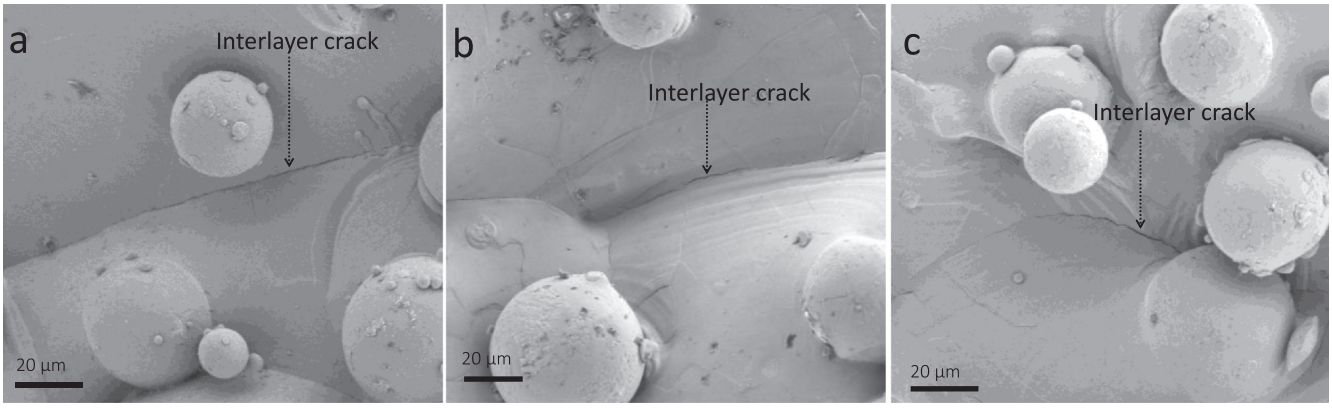

Fig. 11. Interlayer crack on side surface of samples manufactured at scanning speed of 1400 mm.s^{-1} and (a) 300 W and (b and c) 330 W.

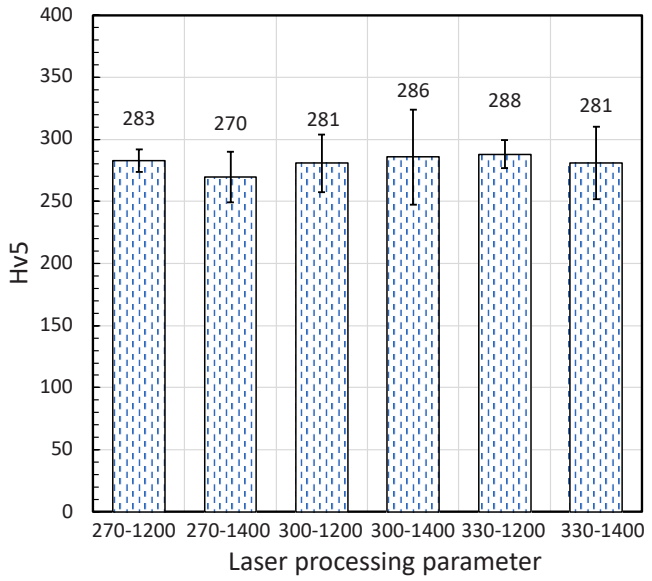

Fig. 12. Vickers hardness number of the top surface of studied samples.

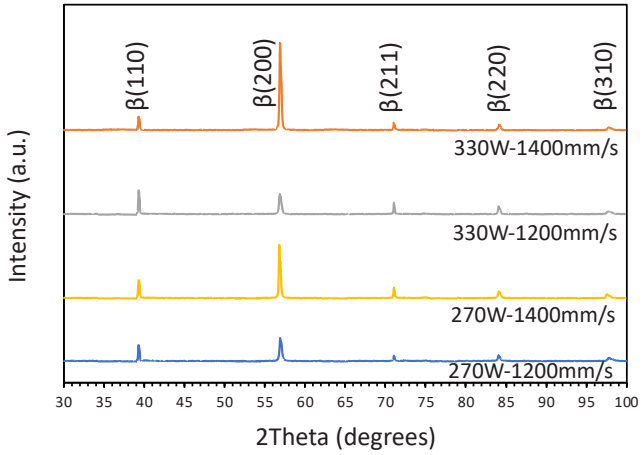

Fig. 13. XRD patterns of the samples investigated in this study.

surrounding on an adhered powder because the indenter slips away from the powder and make the rhombus bigger.

4. Conclusions

Ti-5553 alloy is manufactured using different laser processing parameters employing SLM technique, and the surfaces of the samples are characterised using multiscale techniques. Following outcomes can be summarised below:

1. Surface roughness of side surfaces is measured to be below 20 µm. It is found that in association with laser parameters, raw powder size distribution impact surface quality. Samples produced at 300 W/1200 mm.s^{-1} and 330 W/1200 mm.s^{-1} display least rough surfaces.
2. The adhered powder particles and ripples are observed on the top surfaces of Ti-5553 alloy. Scanning speed significantly impacts these features, for instance, an increase in scanning speed from 1200 to 1400 mm.s^{-1} results in increase in adhered powder particles and ripples appearance. All samples manufactured at 1200 mm.s^{-1} show a good top surface.
3. Side surface is characterised as the presence of adhered powder particles, balling formation, open pore and microcrack. It is found that both scanning speed and laser power affect number of adhered powder particles. At a constant laser power/scanning speed, the number of adhered powder particles increases with increased scanning speed/laser power.
4. Microcrack, an important feature, is found in all conditions. However, more pronouncedly on samples at higher scanning speed and higher powers. Interrelation between laser processing, melt pool viscosity, solidification rate etc determines the cracking in the samples.
5. Vickers hardness value of the SLM processed Ti-5553 alloy shows a range of 270–290 which is in good agreement with traditionally processed materials. The value of VHN also implies that the microstructure of the samples contain single β phase.
6. Overall, samples manufactured using scanning speed of 1200 mm.s^{-1} display better surface quality irrespective of laser power used in this investigation.

CRediT authorship contribution statement

Mansur Ahmed: Conceptualization, Investigation, Formal analysis, Writing – original draft, Funding acquisition. **M.A. Obeidi:** Resources/Instrumentation. **Shuo Yin**: Resources/Instrumentation. **Rocco Lupoi**: Writing – review & editing, Project administration.

Declaration of Competing Interest

The authors declare that they have no known competing financial interests or personal relationships that could have appeared to influence the work reported in this paper.

Acknowledgements

This project has received funding from Enterprise Ireland and the European Union's Horizon 2020 Research and Innovation Programme under the Marie Sklodowska-Curie grant agreement No 847402. Dr. M. Culleton of Trinity College Dublin is thanked for proofread the revised manuscript.

References

[1] N.G. Jones, R.J. Dashwood, D. Dye, M. Jackson, Overcoming barriers to in-hospital cardiac arrest documentation, Mater. Sci. Eng.: A 490 (1) (2008) 369–377.
[2] S.K. Kar, A. Ghosh, N. Fulzele, A. Bhattacharjee, A theoretical study on mathematical modelling of an infectious disease with application of optimal control, Mater. Charact. 81 (2013) 37–48.
[3] S.D. Bartus, Evaluation of Ti-5553 alloy against fragment and armor-piercing projectiles, Report, Army Research Laboratory, September (2009).
[4] J.C. Sabol, T. Pasang, W.Z. Misiolek, J.C. Williams, Localized tensile strain distribution and metallurgy of electron beam welded Ti–5Al–5V–5Mo–3Cr titanium alloys, J. Mater. Process. Technol. 212 (11) (2012) 2380–2385.
[5] D.L. Stewart Veeck, R. Boyer, R. Briggs, Adv. Mater. Process. 162 (10) (2004).
[6] O.M. Ivasishin, D.G. Sawakin, V.S. Moxson, K.A. Bondareval, F.H. Froes, Titanium powder metallurgy for automotive components, Mater. Technol. 17 (1) (2002) 20–25.
[7] C. Micheletti, B.E.J. Lee, J. Deering, D.M. Binkley, S. Coulson, A. Hussanain, H. Zurob, K. Grandfield, Ti-5Al-5Mo-^{5}V-^{3}Cr bone implants with dual-scale topography: a promising alternative to Ti-6Al-4V, Nanotechnology 31 (23) (2020) 235101.
[8] J.P. Kruth, L. Froyen, J. Van Vaerenbergh, P. Mercelis, M. Rombouts, B. Lauwers, Selective laser melting of iron-based powder, J. Mater. Process. Technol. 149 (1) (2004) 616–622.
[9] D.L. Bourell, Int. J. Powder Met. 48 (1993) 369–382.
[10] D.S. Shin, C.H. Lee, U. Kühn, S.C. Lee, S.J. Park, H. Schwab, S. Scudino, K. Kosiba, Optimizing laser powder bed fusion of Ti-5Al-^{5}V-^{5}Mo-3Cr by artificial intelligence, J. Alloy. Compd. 862 (2021) 158018.
[11] D. Sharma, S.R. Kada, D. Fabijanic, D. Parfitt, B. Chen, B. Roebuck, M.E. Fitzpatrick, M.R. Barnett, The ageing response of direct laser deposited metastable β-Ti alloy, Ti–5Al–5Mo–5V–3Cr, Addit. Manuf. 48 (2021) 102384.
[12] H. Schwab, F. Palm, U. Kühn, J. Eckert, Microstructure and mechanical properties of the near-beta titanium alloy Ti-5553 processed by selective laser melting, Mater. Des. 105 (2016) 75–80.

[13] H. Schwab, M. Bönisch, L. Giebeler, T. Gustmann, J. Eckert, U. Kühn, Processing of Ti-5553 with improved mechanical properties via an in-situ heat treatment combining selective laser melting and substrate plate heating, Mater. Des. 130 (2017) 83–89.
[14] M. Khorasani, A. Ghasemi, U.S. Awan, E. Hadavi, M. Leary, M. Brandt, G. Littlefair, W. O'Neil, I. Gibson, A study on surface morphology and tension in laser powder bed fusion of Ti-6Al-4V, Int. J. Adv. Manuf. Technol. 111 (9) (2020) 2891–2909.
[15] W. Tato, L. Blunt, I. Llavori, A. Aginagalde, A. Townsend, A. Zabala, Surface integrity of additive manufacturing parts: a comparison between optical topography measuring techniques, Procedia CIRP 87 (2020) 403–408.
[16] I. Yadroitsev, I. Smurov, Surface morphology in selective laser melting of metal powders, Phys. Procedia 12 (2011) 264–270.
[17] H. Hassanin, A. Elshaer, R. Benhadj-Djilali, F. Modica, I. Fassi, Surface Finish Improvement of Additive Manufactured Metal Parts, in: K. Gupta (Ed.), Micro and Precision Manufacturing, Springer International Publishing, Cham, 2018, pp. 145–164.
[18] D. Obilanade, C. Dordlofva, P. Törlind, Surface roughness considerations in design for additive manufacturing - a literature review, Proc. Des. Soc. 1 (2021) 2841–2850.
[19] B. Li, B. Wang, G. Zhu, L. Zhang, B. Lu, Low-roughness-surface additive manufacturing of metal-wire feeding with small power, Materials 14 (15) (2021) 4265.
[20] S. Demirci, R. Dalmış, T. Dikici, M.M. Tünçay, N. Kaya, A.N. Güllüoğlu, Effect of surface modifications of additively manufactured Ti-6Al-4V alloys on apatite formation ability for biomedical applications, J. Alloy. Compd. 887 (2021) 161445.
[21] A. Sharma, M.C. Oh, J.-T. Kim, A.K. Srivastava, B. Ahn, Investigation of electrochemical corrosion behavior of additive manufactured Ti–6Al–4V alloy for medical implants in different electrolytes, J. Alloy. Compd. 830 (2020) 154620.
[22] Y. Liu, Y. Yang, S. Mai, D. Wang, C. Song, Effects of MgH2-containing precursor addition on the microstructure and mechanical properties of sintered Al alloys, Mater. Des. 87 (2015) 797–806.
[23] N.K. Tolochko, S.E. Mozzharov, I.A. Yadroitsev, T. Laoui, L. Froyen, V.I. Titov, M.B. Ignatiev, Balling processes during selective laser treatment of powders, Rapid Prototyp. J. 10 (2) (2004) 78–87.
[24] Y. Xiang, S. Zhang, Z. Wei, J. Li, P. Wei, Z. Chen, L. Yang, L. Jiang, Forming and defect analysis for single track scanning in selective laser melting of Ti6Al4V, Appl. Phys. A 124 (10) (2018) 685.
[25] C.J. Huang, X.C. Yan, C.Y. Chen, Y.C. Xie, M. Liu, M. Kuang, H.L. Liao, Additive manufacturing hybrid Ni/Ti-6Al-4V structural component via selective laser melting and cold spraying, Vacuum 151 (2018) 275–282.
[26] B. Zhao, H. Wang, N. Qiao, C. Wang, M. Hu, Corrosion resistance characteristics of a Ti-6Al-4V alloy scaffold that is fabricated by electron beam melting and selective laser melting for implantation in vivo, Mater. Sci. Eng.: C 70 (2017) 832–841.
[27] J.J. de Damborenea, M.A. Arenas, M.A. Larosa, A.L. Jardini, C.A. de Carvalho Zavaglia, A. Conde, Corrosion of Ti6Al4V pins produced by direct metal laser sintering, Appl. Surf. Sci. 393 (2017) 340–347.
[28] F. Bartolomeu, S. Faria, O. Carvalho, E. Pinto, N. Alves, F.S. Silva, G. Miranda, Predictive models for physical and mechanical properties of Ti6Al4V produced by selective laser melting, Mater. Sci. Eng.: A 663 (2016) 181–192.
[29] J. Yang, H. Yu, J. Yin, M. Gao, Z. Wang, X. Zeng, Polyimide/mesoporous silica nanocomposites: characterization of mechanical and thermal properties and tribochemistry in dry sliding condition, Mater. Des. 108 (2016) 308–318.
[30] G. Miranda, S. Faria, F. Bartolomeu, E. Pinto, N. Alves, N. Peixinho, M. Gasik, F.S. Silva, A study on the production of thin-walled Ti6Al4V parts by selective laser melting, J. Manuf. Process. 39 (2019) 346–355.
[31] D. Zhang, W. Wang, Y. Guo, S. Hu, D. Dong, R. Poprawe, J.H. Schleifenbaum, S. Ziegler, Numerical simulation in the absorption behavior of Ti6Al4V powder materials to laser energy during SLM, J. Mater. Process. Technol. 268 (2019) 25–36.
[32] T. Vilaro, C. Colin, J.D. Bartout, As-fabricated and heat-treated microstructures of the Ti-6Al-4V alloy processed by selective laser melting, Metall. Mater. Trans. A 42 (10) (2011) 3190–3199.
[33] F. Toptan, A.C. Alves, Ó. Carvalho, F. Bartolomeu, A.M.P. Pinto, F. Silva, G. Miranda, Corrosion and tribocorrosion behaviour of Ti6Al4V produced by selective laser melting and hot pressing in comparison with the commercial alloy, J. Mater. Process. Technol. 266 (2019) 239–245.
[34] K.S. Hamid, S.G. Parekh, S.B. Adams, Salvage of severe foot and ankle trauma with a 3D printed scaffold, Foot Ankle Int. 37 (4) (2016) 433–439.
[35] K. Mumtaz, N. Hopkinson, Top surface and side roughness of Inconel 625 parts processed using selective laser melting, Rapid Prototyp. J. 15 (2) (2009) 96–103.
[36] G. Yu, D. Gu, D. Dai, M. Xia, C. Ma, K. Chang, Influence of processing parameters on laser penetration depth and melting/re-melting densification during selective laser melting of aluminum alloy, Appl. Phys. A 122 (10) (2016) 891.
[37] K.Q. Le, C. Tang, C.H. Wong, On the study of keyhole-mode melting in selective laser melting process, Int. J. Therm. Sci. 145 (2019) 105992.
[38] L. Thijs, F. Verhaeghe, T. Craeghs, J.V. Humbeeck, J.-P. Kruth, A study of the microstructural evolution during selective laser melting of Ti–6Al–4V, Acta Mater. 58 (9) (2010) 3303–3312.
[39] D. Ye, K. Zhu, J.Y.H. Fuh, Y. Zhang, H.G. Soon, Imaging electron-density fluctuations by multidimensional X-ray photon-coincidence diffraction, Opt. Laser Technol. 111 (2019) 395–406.
[40] S. Pal, M. Finšgar, T. Bončina, G. Lojen, T. Brajlih, I. Drstvenšek, Effect of surface powder particles and morphologies on corrosion of Ti-6Al-4 V fabricated with different energy densities in selective laser melting, Mater. Des. 211 (2021) 110184.
[41] C. Zopp, S. Blümer, F. Schubert, L. Kroll, Processing of a metastable titanium alloy (Ti-5553) by selective laser melting, Ain Shams Eng. J. 8 (3) (2017) 475–479.
[42] D. Wang, S. Wu, F. Fu, S. Mai, Y. Yang, Y. Liu, C. Song, Enhanced nucleation and refinement of eutectic Si by high number-density nano-particles in Al–10Si–0.5Sb alloys, Mater. Des. 117 (2017) 121–130.
[43] D. Dai, D. Gu, Protective effect of carnosine on febrile seizures in immature mice, Int. J. Mach. Tools Manuf. 88 (2015) 95–107.
[44] A. Khorasani, I. Gibson, M. Goldberg, G. Littlefair, Production of Ti-6Al-4V acetabular shell using selective laser melting: possible limitations in fabrication, Rapid Prototyp. J. 23 (1) (2017) 110–121.
[45] Z. Chen, Y. Xiang, Z. Wei, P. Wei, B. Lu, L. Zhang, J. Du, Thermal dynamic behavior during selective laser melting of K418 superalloy: numerical simulation and experimental verification, Appl. Phys. A 124 (4) (2018) 313.
[46] T.M. Wischeropp, C. Emmelmann, M. Brandt, A. Pateras, Measurement of actual powder layer height and packing density in a single layer in selective laser melting, Addit. Manuf. 28 (2019) 176–183.
[47] L.-z Wang, S. Wang, J.-j Wu, Experimental investigation on densification behavior and surface roughness of AlSi10Mg powders produced by selective laser melting, Opt. Laser Technol. 96 (2017) 88–96.
[48] A. Azarniya, X.G. Colera, M.J. Mirzaali, S. Sovizi, F. Bartolomeu, Mk Weglowski St, W.W. Wits, C.Y. Yap, J. Ahn, G. Miranda, F.S. Silva, H.R. Madaah Hosseini, S. Ramakrishna, A.A. Zadpoor, Additive manufacturing of Ti–6Al–4V parts through laser metal deposition (LMD): process, microstructure, and mechanical properties, J. Alloy. Compd. 804 (2019) 163–191.
[49] D.A. Brice, P. Samimi, I. Ghamarian, Y. Liu, R.M. Brice, R.F. Reidy, J.D. Cotton, M.J. Kaufman, P.C. Collins, Oxidation behavior and microstructural decomposition of Ti-6Al-4V and Ti-6Al-^{4}V–^{1}B sheet, Corros. Sci. 112 (2016) 338–346.
[50] V.C. Opini, C.A.F. Salvador, K.N. Campo, E.S.N. Lopes, R.R. Chaves, R. Caram, α phase precipitation and mechanical properties of Nb-modified Ti-5553 alloy, Mater. Sci. Eng.: A 670 (2016) 112–121.
[51] S. Bakhshivash, H. Asgari, P. Russo, C.F. Dibia, M. Ansari, A.P. Gerlich, E. Toyserkani, Printability and microstructural evolution of Ti-5553 alloy fabricated by modulated laser powder bed fusion, Int. J. Adv. Manuf. Technol. 103 (9) (2019) 4399–4409.